Inorganic Chemistry
Article
pubs.acs.org/IC

Magnetic Transitions in Iron Porphyrin Halides by Inelastic Neutron Scattering and Ab Initio Studies of Zero-Field Splittings

Shelby E. Stavretis,[†] Mihail Atanasov,[*,‡,§] Andrey A. Podlesnyak,[*,∥] Seth C. Hunter,[†] Frank Neese,[*,‡] and Zi-Ling Xue[*,†]

[†]Department of Chemistry, The University of Tennessee, Knoxville, Tennessee 37996, United States
[‡]Max Planck Institute for Chemical Energy Conversion, Stiftstraße 34-36, D-45470 Mülheim an der Ruhr, Germany
[§]Institute of General and Inorganic Chemistry, Bulgarian Academy of Sciences, 1113 Sofia, Bulgaria
[∥]Quantum Condensed Matter Division, Oak Ridge National Laboratory, Oak Ridge, Tennessee 37831, United States

Ⓢ *Supporting Information*

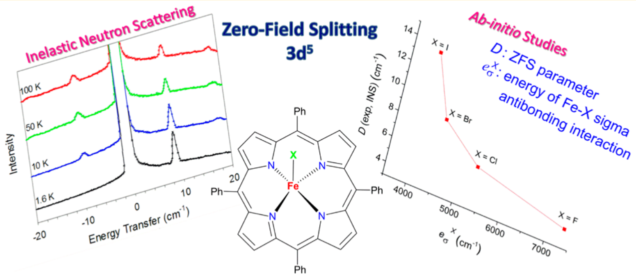

ABSTRACT: Zero-field splitting (ZFS) parameters of nondeuterated metalloporphyrins [Fe(TPP)X] (X = F, Br, I; H_2TPP = tetraphenylporphyrin) have been directly determined by inelastic neutron scattering (INS). The ZFS values are D = 4.49(9) cm^{-1} for tetragonal polycrystalline [Fe(TPP)F], and D = 8.8(2) cm^{-1}, E = 0.1(2) cm^{-1} and D = 13.4(6) cm^{-1}, E = 0.3(6) cm^{-1} for monoclinic polycrystalline [Fe(TPP)Br] and [Fe(TPP)I], respectively. Along with our recent report of the ZFS value of D = 6.33(8) cm^{-1} for tetragonal polycrystalline [Fe(TPP)Cl], these data provide a rare, complete determination of ZFS parameters in a metalloporphyrin halide series. The electronic structure of [Fe(TPP)X] (X = F, Cl, Br, I) has been studied by multireference ab initio methods: the complete active space self-consistent field (CASSCF) and the N-electron valence perturbation theory (NEVPT2) with the aim of exploring the origin of the large and positive zero-field splitting D of the $^6A_1$ ground state. D was calculated from wave functions of the electronic multiplets spanned by the d^5 configuration of Fe(III) along with spin−orbit coupling accounted for by quasi degenerate perturbation theory. Results reproduce trends of D from inelastic neutron scattering data increasing in the order from F, Cl, Br, to I. A mapping of energy eigenvalues and eigenfunctions of the $S = 3/2$ excited states on ligand field theory was used to characterize the σ- and π-antibonding effects decreasing from F to I. This is in agreement with similar results deduced from ab initio calculations on CrX_6^{3-} complexes and also with the spectrochemical series showing a decrease of the ligand field in the same directions. A correlation is found between the increase of D and decrease of the π- and σ-antibonding energies e_λ^X ($\lambda = \sigma, \pi$) in the series from X = F to I. Analysis of this correlation using second-order perturbation theory expressions in terms of angular overlap parameters rationalizes the experimentally deduced trend. D parameters from CASSCF and NEVPT2 results have been calibrated against those from the INS data, yielding a predictive power of these approaches. Methods to improve the quantitative agreement between ab initio calculated and experimental D and spectroscopic transitions for high-spin Fe(III) complexes are proposed.

■ INTRODUCTION

The chemistry of metalloporphyrins has the potential to impact our understanding of biological and geological roles that the naturally occurring systems play.[1−3] The diverse biological functions of heme proteins are often attributed to the varying degree of changes in the local heme environment as shown in Table 1.[1,3] Many metalloporphyrins have unpaired electrons, making the compounds paramagnetic. One intrinsic property in paramagnetic compounds is the zero-field splitting (ZFS). For compounds with spin $S \geq 1$, the interaction of the electron spins mediated by spin−orbital coupling (SOC) leads to a splitting of the spin states of otherwise degenerate states.[4−6] The spin Hamiltonian up to second-rank terms is given in eq 1:[7]

$$\hat{H}_s = D\left[\hat{S}_z^2 - \frac{1}{3}S(S+1)\right] + E\left[\hat{S}_x^2 - \hat{S}_y^2\right] \qquad (1)$$

where D and E are the axial and rhombic ZFS parameters, respectively, which measure the magnetic anisotropy of the system. When the x and y directions are equivalent, E = 0.

ZFS manifests as differences among energy levels in the absence of an external magnetic field. For d^5 Fe(III) porphyrin complexes in the current studies, the electronic ground states of complexes with S = 5/2 are split as shown in Scheme 1. The resulting energy spectrum exhibits peaks, $2D$ and $4D$, that are associated with transitions in ZFS. The rhombic ZFS, E, mixes

Received: July 6, 2015

DOI: 10.1021/acs.inorgchem.5b01505
Inorg. Chem. XXXX, XXX, XXX−XXX

Table 1. Comparison of D (cm^{-1}) Values of Different Fe(III) Porphyrin Halides Determined by Different Methods

X	[Fe(TPP)X] by other methods	[Fe(TPP)X] by INS including the current work	Fe(III) protoporphyrin IX dimethyl ester halides (Chart 1) by far-IR	Fe(III) deuteroporphyrin IX dimethyl ester halides by far-IR
F		4.49(9)	5.0(1)[12]	5.55(11)[12]
Cl	6.5 (far-IR),[17] D = 3.2−11.9 determined by other methods[11]	6.33(8)[11]	6.95(14)[12]	8.95(18)[12]
Br	4.9 (magnetic susceptibility),[15b] 9.15 (far-IR),[17] 12.5(5) (magnetic susceptibility)[15a,16]	8.8(2)	9.75[17]	11.80(23)[12]
I	13.5(5) (magnetic susceptibility)[16]	13.4(6)	14.5[17]	16.40(15)[12]

Scheme 1. (a) Structures of Metalloporphyrins in the Current Studies; (b) d Orbital Splitting; (c) and (d) ZFS in Compounds with $S = 5/2$ with $D > 0$, $E = 0$ (for $D < 0$, Energy Levels Will Be Inverted), and $E \neq 0$, Mixing of Pure Doublet States ($E \ll D$)[4a]

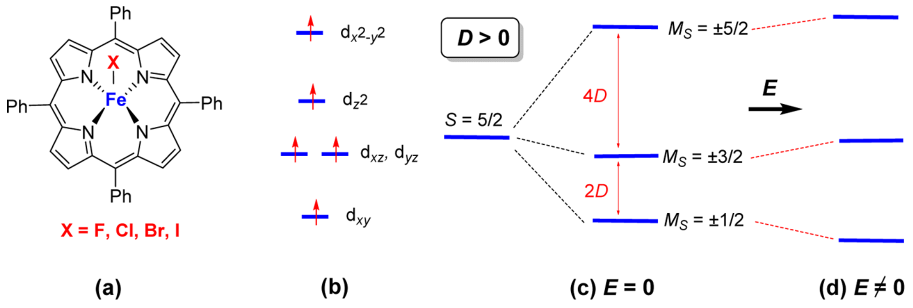

the $\Delta M_S = \pm 2$ states. Thus, the $M_S = \pm 1/2$ states interact with either $M_S = \pm 5/2$ or $\mp 3/2$ states, leading to the shift of the energy levels shown in Scheme 1d.

ZFS is of fundamental importance to understanding molecular magnetism. While ZFS parameters have been actively studied, there is still a limited understanding on how ZFS parameters relate to the geometric and electronic structures of transition metals compounds, including how metal−ligand bonding affects ZFS.[4,5] Knowledge of the effects of metal−ligand bonding on ZFS also helps design better single molecular magnets (SMMs) as data storage and quantum computing materials.[8]

ZFS, including that of metalloporphyrins, has been investigated by several techniques, including high-field and high-frequency electron paramagnetic resonance (HFEPR), magnetic susceptibility measurement, nuclear magnetic resonance (NMR), far-infrared (far-IR), Mössbauer spectroscopy, magnetic circular dichroism (MCD), and inelastic neutron scattering (INS).[1,6,9,10] INS is one of the few techniques that directly gives both the magnitude of the D parameter and often its sign. Because of its spin, neutrons carry a magnetic moment that makes them an excellent probe for the investigation of magnetic structures and dynamics. There is a strong interaction between magnetic field (magnetization density) created by the unpaired electrons in the sample and magnetic moment of the neutron. Incident neutrons are scattered from the magnetization density of the atom. The effect of ZFS on a transition metal ion is to partially or totally remove the $(2S + 1)$-fold degeneracy of the ground-state multiplet. In the case of d^5 Fe(III) compounds with ZFS in Scheme 1, the magnetization density that interacts with the spin of neutrons is the spin dipole moment from the 5 unpaired d electrons, as the orbital angular momentum of the d electrons in the complexes is quenched. The resulting energy spectrum exhibits peaks associated with transitions from $M_S = \pm 1/2$ to $\pm 3/2$ ($2D$) and from $M_S = \pm 3/2$ to $\pm 5/2$ ($4D$) in Scheme 1.

To our knowledge, few bioinorganic complexes have been studied by INS. We recently reported the direct determination of ZFS parameters of several nondeuterated metalloporphyrins [M(TPP)Cl] (M = Fe, Mn, Cr) and [Mn(TPP)] (H_2TPP = tetraphenylporphyrin).[11] With the nature of how ligands affect ZFS relatively unknown, the current study focuses on iron(III) porphyrin halides, which are common inorganic ligands, with a 2-fold interest: (a) The first is determination of ZFS parameters for [Fe(TPP)X] (X = F, Br, and I) by INS. Thus, along with [Fe(TPP)Cl], a compound we recently studied,[11] this is a rare complete series of biomimetic halide compounds with the ZFS values determined.[12] (b) The second is ab initio study of the electronic structure and magnetic anisotropy of the metalloporphyrins to explore the origin of the large and positive zero-field splitting of the $^6A_1$ ground state.

There have been many previous studies of the ZFS of Fe(III) compounds with a $^6A_1$ ground state. Solomon and co-workers have investigated the origin of the $^6A_1$ ground-state zero-field splitting in axially distorted high-spin d^5 $[FeCl_4]^-$.[5] Brackett and co-workers have reported D values of four Fe(III) deuteroporphyrin IX dimethyl ester halides (Chart 1) that were determined by far-IR (Table 1).[12] Goff and co-workers have reported correlations of axial ligand field strength and zero-field splittings in the C-13 NMR spectra of 5- and 6-coordinate high-spin Fe(III) porphyrin complexes.[13] Ohya and Sato conducted a comparative study of Mössbauer spectra of

Chart 1

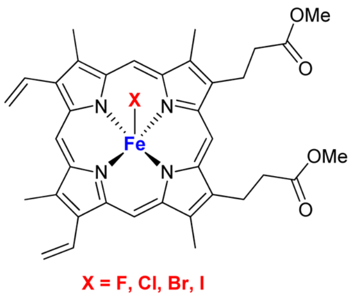

Fe(III) protoporphyrin IX dimethyl ester halides three halides [Fe(TPP)X] (X = Cl, Br, I) to probe electronic effects of substituents and axial ligands.[14] In addition, *D* parameters of [Fe(TPP)Br] and [Fe(TPP)I] have been determined by magnetic susceptibility measurements (Table 1).[15,16] For [Fe(TPP)Br], $D = 13.0(5)$ cm^{-1} was reported initially[15a] and later revised to 12.5(5) cm^{-1} based on reanalysis of the data. For [Fe(TPP)I], the reported $D = 13.5(5)$ cm^{-1}.[16] Far-IR studies by Uenoyama gave $D = 9.15$ cm^{-1} for [Fe(TPP)Br] (Table 1).[17] To our knowledge, ZFS of [Fe(TPP)F] has not been studied.

Although both [Fe(TPP)Br] and [Fe(TPP)I] molecules have 4-fold symmetry, their crystals are in the monoclinic system. Thus, the rhombic parameter *E* in eq 1 is required to explain ZFS properties of their crystalline samples. However, the earlier determination of ZFS parameters by magnetic susceptibility measurements and far-IR did not determine the *E* values.[15,17] Several experimental measurements, such as magnetic susceptibility and HFEPR, that allow for the determination of the *g*-factor require the use of a magnetic field, which prevents direct measurement of zero-field splitting (ZFS).

INS has been used to probe the magnetic properties of metal complexes, especially excitations among low-lying energy levels.[18] For example, the low-lying energy levels of magnetic clusters have been characterized by INS.[4,18] *D* for single-molecule magnets $[Mn_4O_3X(OAc)_3(dbm)_3]$ ($X = Br^-$, Cl^-, OAc^-, and F^-) have been studied by Güdel and co-workers to see how the *D* values change with the axial X^- ligands.[18b] The state-of-the-art facilities at Spallation Neutron Source (SNS) at Oak Ridge National Laboratory (U.S.) have made it possible to probe magnetic properties of nondeuterated metal complexes in detail.[18e] We have used the cold neutron chopper spectrometer (CNCS)[19] at SNS to determine both the size and the sign of ZFS parameters *D* for nondeuterated metalloporphyrins [Fe(TPP)X] (X = F, Br, and I) as well as the best fit *E* values for [Fe(TPP)X] (X = Br, I). In addition, we have calculated the electronic structure of [Fe(TPP)X] (X = F, Cl, Br, I) with a $^6A_1$ ground state by multireference ab initio methods to explore the origin of their *D* values. A correlation is found between the increase of *D* and the decrease of the π- and σ-antibonding energies e_λ^X ($\lambda = \sigma, \pi$) in the series from X = F to I. Analysis of this correlation using second-order perturbation theory expressions in terms of angular overlap parameters allows one to rationalize the experimentally deduced trends.

■ EXPERIMENTAL SECTION

Synthesis of [Fe(TPP)X] (X = F, Br, I). [Fe(TPP)X] were prepared by following a literature method[20] with modifications. Details of our syntheses of [Fe(TPP)X] (X = F, Br, I) are given in the Supporting Information.[13,15b,20] The overall synthesis is shown in Scheme 2.

Air-stable solid products of [Fe(TPP)X] (X = F, Br, I) were characterized by UV−visible spectroscopy and powder X-ray diffraction. Powder diffraction patterns were obtained on the PANalytical Empyrean diffractometer using Cu K_α radiation ($\lambda = 1.5418$ Å) with samples of [Fe(TPP)X] (X = F, Br, I) on a zero-background plate holder. Powder X-ray diffraction of the [Fe(TPP)F] sample is consistent with the simulated pattern predicted from the single-crystal X-ray diffraction data of [Fe(TPP)Cl] (Figure S2).[21] We could not use the reported single-crystal X-ray structure of [Fe(TPP)F], as some key data are not available.[22] The reported crystal structure does, however, indicate that the solid sample is in the tetragonal crystal system,[22] as the crystal structure of [Fe(TPP)Cl].[21] Indexing of our powder X-ray diffraction data from the [Fe(TPP)F] sample by the McMaille method also yielded the same tetragonal unit cell.[23]

Scheme 2. Synthesis of [Fe(TPP)X] (X = F, Br, I)

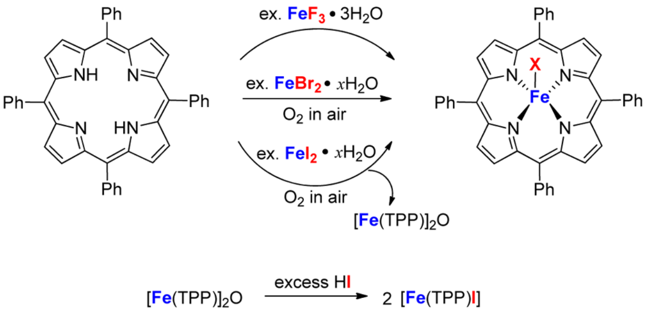

The powder X-ray diffraction of the [Fe(TPP)Br] sample is consistent with the simulated pattern predicted from the single-crystal X-ray diffraction data of [Fe(TPP)Br],[24] indicating that the solid sample is in the monoclinic crystal system. It should be noted that Skelton and White originally reported the structure in $P2_1/c$ [$a = 10.191(2)$, $b = 16.121(5)$, $c = 23.223(4)$ Å, $\beta = 115.34(1)°$].[24a] This space group could be converted to $P2_1/n$.[24b] Conversion by the matrix and software at http://www.cryst.ehu.es/cryst/celltran.html (using a primitive *P* cell) yields $P2_1/n$, $a = 10.191(2)$, $b = 16.121(5)$, $c = 20.990(4)$ Å, $\beta = 90.69(1)°$.

The powder X-ray diffraction of the [Fe(TPP)I] sample is consistent with the simulated pattern predicted from the single-crystal X-ray diffraction data of [Fe(TPP)I] [$P2_1/n$, $a = 10.118(3)$, $b = 16.352(4)$, $c = 21.211(7)$ Å, $\beta = 89.56(2)°$],[25] indicating that the sample is also in the monoclinic crystal system.

Because INS peaks other than the two expected magnetic transitions were observed for [Fe(TPP)Br] and [Fe(TPP)I] as discussed below, elemental analyses of the two samples were performed (Supporting Information), confirming the purity of the samples. Attempts to obtain mass spectra of [Fe(TPP)X] (X = F, Br, I) by MALDI/TOF (matrix assisted laser desorption ionization time-of-flight) led to the observation of $[Fe(TPP)^+]$, indicating dissociation of the Fe−X bonds during the mass spectroscopic process (Supporting Information).

INS Studies of [Fe(TPP)X] (X = F, Br, I). The INS measurements were carried out on the CNCS, which is a direct geometry, time-of-flight spectrometer that receives a beam from a coupled cryogenic H_2 moderator.[19] For energy selection, the CNCS employs four chopper assemblies. The speeds and slit widths of the choppers can be varied, allowing adjustments in the instrumental resolution and intensity of the incident beam. Approximately 500 mg of each sample was loaded into a 1/2-in.-thick aluminum tube. The three tubes, containing [Fe(TPP)X] (X = F, Br, I) each, were placed in a sample holder. The sample holder was mounted in a standard liquid helium cryostat with a base temperature of $T = 1.6$ K. An oscillating radial collimator was used to reduce background scattering form the tail of the cryostat. Vanadium was used as a standard for the detector efficiency correction.

The incident neutron energy for every measurement was chosen to cover the anticipated region of interest in both the energy *E* and scattering-vector *Q* space.[26,27] The small incident energy is especially important to observe excitations near the elastic peak (at energy transfer close to 0 cm^{-1}), as the full-width-at-half-maximum (fwhm) of the elastic peak, which is typically 1.5−2% of the incident energy, would be narrow, giving better energy resolution.

For [Fe(TPP)F], measurements were performed at 1.6, 10, 50, and 100 K with incident neutron beam energies $E_i = 24.20$, 40.89, and 97.35 cm^{-1}. For [Fe(TPP)Br] and [Fe(TPP)I], measurements were performed at 1.6, 10, and 50 K with $E_i = 24.20$, 40.89, and 97.35 cm^{-1}. It took approximately 24 h to run the three samples at various temperatures and incident neutron energies. Data were then reduced and analyzed using the DAVE (Data Analysis and Visualization Environment) program package.[28]

Table 2. Experimental (X-ray Diffraction, X = F, Cl, Br, I; Neutron Diffraction, X = Cl) versus DFT Structural Parameters of the [Fe(TPP)X] (X = F, Cl, Br, I) Complex Series

	F		Cl		Br		I	
X	X-ray	DFT	X-ray[21]/neutron	DFT	X-ray[24a]	DFT	X-ray[25]	DFT
Fe–X (Å)		1.815	2.194/2.200	2.210	2.348	2.360	2.554	2.566
Fe–N (Å)		2.063	2.052/2.067	2.061	2.069	2.057	2.061	2.054
					2.074		2.076	
					2.057		2.055	
					2.078		2.074	
∠XFeN (deg)		102.78	100.99/101.96	102.89	104.10	102.37	102.94	101.86
					103.89		103.38	
					103.67		103.26	
					103.04		101.83	

For [Fe(TPP)Br] and [Fe(TPP)I], a pair of D and E values were used to give a calculated INS spectrum, which was then compared to the experimental INS spectrum to find the best fit. The D, E values were determined through the use of the chi-square goodness of fit test of the experimental and calculated INS peaks.

The line widths of the INS peaks lie within experimental accuracy determined by the instrumental resolution. The effective resolution function $R(Q,E)$ of CNCS is nearly Gaussian in energy.[19] Therefore, the INS intensities were fit assuming Gaussian line shapes with fwhm of the energy resolution for the CNCS spectrometer. The detailed analyses, using the plots with smaller stepsize points, and calculations of errors in the D values, are given in the Supporting Information.

Computational Details. *Coordination Geometries.* Although the crystal structures of four [Fe(TPP)X] complexes in this study have been reported (X = F,[22] Cl,[21] Br,[24a] and I[25]), only atomic coordinates for the structures of X = Cl, Br, and I are available. In addition, the structure of X = Cl is disordered.[25] Therefore, for the sake of our analysis, we have used DFT geometries for all four complexes. Calculations for the available experimental structures show no major differences (Table S7). DFT geometry optimization of all four [Fe(TPP)X] (X = F, Cl, Br, I) complexes was done with the BP86 functional and def2-TZVP basis sets. van der Waals correction for nonbonding interactions was included following Grimme.[29,30] Because of the participation of heavy ligands in the coordination sphere of Fe(III), scalar relativistic corrections were included with the Douglas–Kroll–Hess method along with appropriate basis sets.[31] Structural parameters from these computations are compared to X-ray data in Table 2.

Electronic Multiplets and the Zero-Field Splitting Parameters D. The d^5 configuration of Fe^{III} gives rise to one $S = 5/2$ ground (6 microstates) and to 24 $S = 3/2$ (96 microstates) and 75 $S = 1/2$ (150 microstates) electronically excited states. Because the SOC operator connects only ΔS, $\Delta L = 0, \pm 1$ states, the spin-components of the $S = 1/2$ states do not couple to the $S = 5/2$ ground state and have been neglected. Nonrelativistic energy levels and wave functions have been computed using the Complete-Active-Space-Self-Consistent Field (CASSCF) method,[32] averaging over the electron densities of all considered states and taking an active space with 5 electrons distributed over the 5 3d-MOs [CAS(5,5)]. Dynamical (short-range) correlation effects were accounted for by using N-electron valence perturbation theory to second order (NEVPT2).[33−37] The effect of NEVPT2 on the energy levels is to replace the diagonal matrix elements of the configuration interaction (CI) matrix given by CASSCF with improved diagonal energies. Such a replacement provides more accurate (but still approximate) energetics while keeping the same (zeroth-order) CASSCF wave functions. CASSCF and NEVPT2 methods have been efficiently implemented in the program package ORCA[38,39] and allow computations on real systems (without the necessity of model truncations) with unprecedented size (up to 100–200 atoms, 2000 contracted basis functions). From the resulting energies of many-electron states, spin-Hamiltonian parameters were computed applying a computational protocol described elsewhere.[40] To this end, SOC was taken into account using a mean-field spin–orbit coupling operator.[41,42] Spin–orbit mixing of nonrelativistic CI eigenfunctions and splitting of the corresponding eigenvalues are accounted for by Quasi Degenerate Perturbation Theory (QDPT).[42] In these, as well as in the correlated calculations, triple-ζ valence quality basis sets (def2-TZVP)[43,44] were used. Ground-state ZFS parameters have been computed by diagonalizing the state interaction SOC matrix nonperturbatively using effective Hamiltonian theory. CASSCF and NEVPT2 energies for the lowest 17 excited states are listed in Tables S5 and S6.

Metal ligand antibonding energies have been derived using the angular overlap model (AOM)[45,46] of the ligand field with parameters that have been obtained from a least-squares fit to 5 × 5 ligand field matrixes resulting from the ab initio ligand field theory (AILFT) method.[47,48] Inter electronic repulsion between the 3d-electrons has been modeled in terms of two Racah parameters B and C. AOM calculations were carried out with the AOMX program.[49]

■ RESULTS AND DISCUSSION

INS Studies. Neutron magnetic scattering cross-section corresponds to the number of neutrons scattered per second, due to the magnetic interaction described above, into a solid angle dΩ with energy transfer between $\hbar\omega$ and $\hbar(\omega + d\omega)$, divided by the flux of the incident neutrons. For unpolarized neutrons, identical magnetic ions with localized electrons, and spin-only scattering, the magnetic scattering cross-section is expressed by eq 2:[26,27]

$$\frac{d^2\sigma}{d\Omega\, d\omega} = (\gamma r_0)^2 \frac{k_f}{k_i}\left[\frac{1}{2} g F(\mathbf{Q})\right]^2 e^{-2W(\mathbf{Q})} \sum_{\alpha,\beta}\left(\delta_{\alpha\beta} - \frac{\mathbf{Q}_\alpha \cdot \mathbf{Q}_\beta}{Q^2}\right) S^{\alpha\beta}(\mathbf{Q}, \omega) \quad (2)$$

where σ is the neutron cross section; γ is the gyromagnetic ratio, r_0 is the classical radius of an electron, g is the Landé g-factor, $F(\mathbf{Q})$ is the dimensionless magnetic form factor defined as the Fourier transform of the normalized spin density associated with magnetic ions; $e^{-2W(\mathbf{Q})}$ is the Debye–Waller factor caused by thermal motion; $S^{\alpha\beta}(\mathbf{Q},\omega)$ is the magnetic scattering function; $(\delta_{\alpha\beta} - (\mathbf{Q}_\alpha \mathbf{Q}_\beta)/Q^2)$ is the polarization factor, which implies neutrons can only couple to magnetic moments or spin fluctuations perpendicular to $\mathbf{Q}$; $\mathbf{Q}$ is the scattering vector of the momentum transfer (Scheme 3)—For powder samples, only the length Q is measured; $\hbar\omega$ is the energy change experienced by the sample; and ω is the angular frequency of neutron.

In eq 2, the magnetic form factor $F(\mathbf{Q})$ reveals the distribution of spin and orbital magnetization from unpaired electrons. It falls off with increased Q. Therefore, peaks of magnetic origin decrease in intensity with increased Q. In

Scheme 3. Schematic of the INS Process[a]

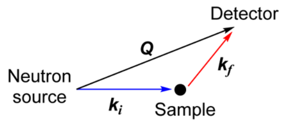

[a] **Q** = $\mathbf{k}_i - \mathbf{k}_f$ is the scattering vector of the momentum transfer, where $\mathbf{k}_i$ and $\mathbf{k}_f$ refer to the wavevectors of the incoming and outgoing neutrons, respectively.

contrast, peaks of vibrational origin increase with increased Q. However, strong incoherent scattering from samples containing hydrogen atoms may smear out Q dependence of the magnetic peaks, and instrumentation constraints might limit the accessible Q range, leading to roughly constant intensities of the magnetic peaks throughout the observable Q range in the samples.[18b,g]

Peak position in INS spectra gives a direct measurement of the eigenvalues of the spin Hamiltonian. When there is no external magnetic field and the compound is in the tetragonal environment, the spin Hamiltonian is defined by a single anisotropy parameter D and depends on the spin projection along z. The E parameter provides a distortion that removes the axial symmetry, and introduces anisotropy in the xy plane. For [Fe(TPP)X], two magnetic INS peaks are observed, as discussed below. The D and E parameters were then determined from the spin Hamiltonian in eq 1 using INS data, as described in the Experimental Section.

Simulated INS spectra were obtained by calculating the energies and corresponding wave functions via exact diagonalization of the spin Hamiltonian expressed in eq 1. These calculations can be used to get the INS intensity, which is proportional to the scattering function $S^{\alpha\beta}(\mathbf{Q},\omega)$. The experimental and simulated INS spectra are given for comparison.

[Fe(TPP)F]. In [Fe(TPP)F], the Fe(III) ion has a high spin ($S = 5/2$) configuration, and its electronic ground state is split into three Kramers doublets: $M_s = \pm 1/2$, $\pm 3/2$, and $\pm 5/2$ (Scheme 1). The spacings among the three doublets are $2D$ and $4D$, respectively. In the INS spectra of [Fe(TPP)F], a peak at 8.99 cm^{-1} was observed (Figure 1) at 1.6, 10, 50, and 100 K. This peak corresponds to the first excitation from the $M_s = \pm 1/2$ to the $M_s = \pm 3/2$ states. Magnetic intensities are based on Boltzmann statistics. Therefore, as the temperature is increased, the $2D$ peak decreases in intensity, as shown in Figure 1. In addition, the first excited states are populated with the temperature increase. The excitation from the first excited, $M_s = \pm 3/2$ states to the second excited, $M_s = \pm 5/2$ states produced the second, $4D$ peak. This peak is observed at 18.05 cm^{-1}, which is approximately twice the energy (8.99 cm^{-1}) of the $2D$ peak. The intensity of the $4D$ peak increases with temperature, indicating its magnetic origin. Analyses of the temperature dependence of experimental and calculated intensities are given in Figures S6−S8.

INS may also give the sign of D for these $S = 5/2$ systems. Because the $2D$ peak was observed at a low temperature before the $4D$ peak, the axial D parameters of these complexes (X = F, Br, I) are positive. If $D < 0$, the ground state would be $M_s = \pm 5/2$ and the first peak observed at 1.6 K would be $4D$ (Scheme 1c).

In addition, peaks with negative energy transfers were also observed in INS. When the temperature was raised to 10 K, a peak at −8.99 cm^{-1} appeared, indicating that the incident neutrons gained energy from the sample in the INS process. In other words, molecules at the ±3/2 states in Scheme 1 returned to the ground ±1/2 states, transferring the energy to the neutrons. Thus, the ZFS parameters are $D = 4.49(9)$ cm^{-1} and $E = 0$ cm^{-1}. The error analysis is given in the Supporting Information.

[Fe(TPP)Br]. The E parameter in the monoclinic crystals of [Fe(TPP)Br] leads to a change of the energy levels in Scheme 1d. The transitions from $M_S = \pm 1/2$ to $\pm 3/2$ and from $M_S = \pm 3/2$ to $\pm 5/2$ ($E \ll D$) are no longer $2D$ and $4D$, respectively.[4a] There is now an E component inside these transitions that is not independent of D. Experimentally, the energy of the $4D$ peak is very close to twice the energy of the $2D$ peak, demonstrating that this compound is close to the axial symmetry with a small E value. (See Figure 4 to view how E affects the energy levels of $S = 5/2$ compounds.) The INS spectra of [Fe(TPP)Br] are given Figure 2. The first and second magnetic peaks are located at ±17.5 and 35.04 cm^{-1}, respectively. Thus, the ZSF parameters are $D = 8.8(2)$ and $E = 0.1(2)$ cm^{-1}. A comparison of the temperature dependence of experimental and calculated intensities, given in Figures S11−S13, confirms the magnetic nature of the peaks. Other peaks (~11.5 and 26 cm^{-1}) in the spectra have different line widths. In comparison to the magnetic peaks, they are broader and not well shaped. The differences suggest that the peaks are not due to transitions from well-determined energy levels but rather from phonon density of states. This argument is confirmed by comparing how the intensities of the peaks change with different Q ranges with low to high Q values. The peaks at 11.5

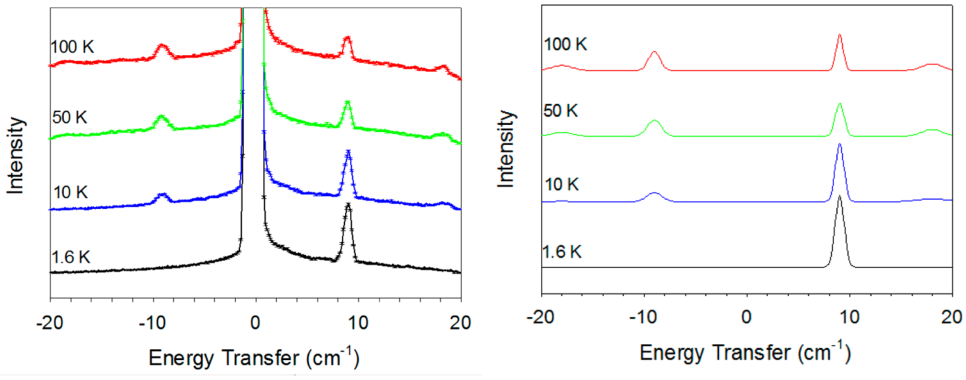

Figure 1. (Left) INS spectra of [Fe(TPP)F] with incident neutron energy $E_i = 24.20$ cm^{-1}, $Q = 0.5$−1.3 Å^{-1}, and a step size of 0.024 cm^{-1}. (Right) Theoretical INS spectra of an $S = 5/2$ spin system with $D = 4.49$ cm^{-1}.

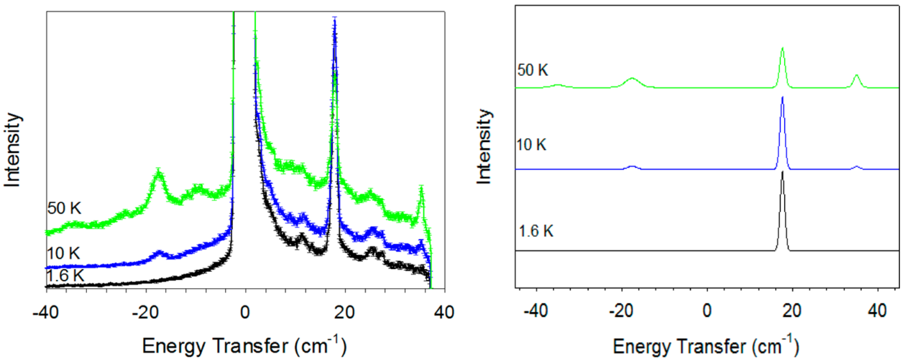

Figure 2. (Left) INS spectra of [Fe(TPP)Br] with E_i = 40.89 cm^{-1}, Q = 0.48−1.8 Å^{-1}, and a step size of 0.016 cm^{-1}. (Right) Theoretical INS spectra of an S = 5/2 spin system with D = 8.8 cm^{-1} and E = 0.1 cm^{-1}.

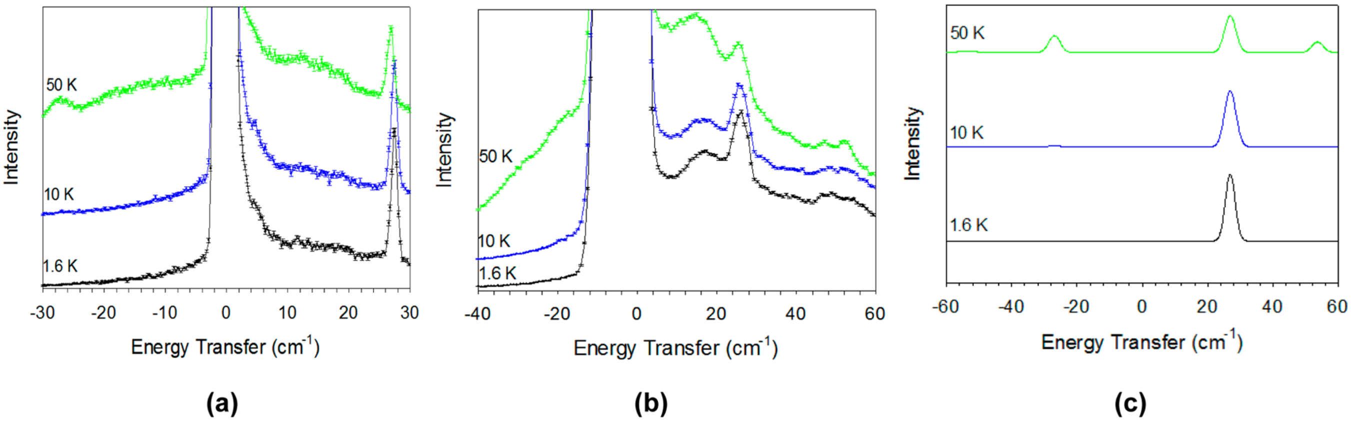

(a) (b) (c)

Figure 3. (a) INS spectra of [Fe(TPP)I] with E_i = 40.89 cm^{-1}, Q = 0.5−1.0 Å^{-1}, and a step size of 0.024 cm^{-1}. (b) INS spectra with E_i = 97.35 cm^{-1}, Q = 0.48−1.8 Å^{-1}, and a step size of 0.024 cm^{-1}. (c) Theoretical INS spectra of an S = 5/2 spin system with D = 13.4 cm^{-1} and E = 0.3 cm^{-1}.

and 26 cm^{-1} were identified as phonons as they have the greatest intensities at high Q as shown in Figure S14. It should be noted that, in addition to a magnetic peak at 18.3 cm^{-1} (Table 1), Uenoyama also observed the 11.5 cm^{-1} peak, which was not identified in the far-IR spectrum of [Fe(TPP)Br].[17]

[Fe(TPP)I]. Two incident energies had to be used to observe two magnetic transitions in the INS spectra. An incident neutron energy of E_i = 40.89 cm^{-1} only displayed the first magnetic peak at 26.8 cm^{-1} (Figure 3a). At a higher incident energy E_i = 97.35 cm^{-1}, the second magnetic peak at 53.3 cm^{-1} appeared (Figure 3b). Analysis of the INS spectra for [Fe(TPP)I] and the determination of ZFS parameters were analogous to those for [Fe(TPP)Br]. The temperature dependence of experimental and calculated intensities is shown in Figure S17. The second magnetic peak is broad and almost overlaps with a phonon peak, meaning this magnetic peak is not as resolved as the first due to the proximity of a phonon peak. Therefore, there is a larger error associated with the use of this peak to calculate the D and E parameters. Equation 1 gave the ZFS parameters D = 13.4(6) cm^{-1} and E = 0.3(6) cm^{-1}. As [Fe(TPP)Br], the spectra for [Fe(TPP)I] also have additional peaks with broad line widths, which were determined to be from phonon density states. The presence of phonon peaks is confirmed by examining the Q dependence of the peaks in Figures S18,S19. As expected, the phonon peaks are more pronounced at high Q, while the magnetic peaks stay constant or decrease in intensity.

Both [Fe(TPP)Br] and [Fe(TPP)I] have a small E value. This in turn translates into small variations of the 2D and 4D peak positions. When the E parameter is small, there is little mixing of the energy levels until E > 2 cm^{-1} as observed in Figure 4. For example, in [Fe(TPP)I] with D = 13.4 cm^{-1}, changing from E = 0 to 0.3 cm^{-1} leads to a 0.58% increase and 0.11% decrease in the positions of the 2D and 4D peaks, respectively.

The D values for [Fe(TPP)X] (X = F, Cl,[11] Br, I) from the INS studies are listed in Table 1. D values of [Fe(TPP)X], determined by other methods, and Fe(III) protoporphyrin/

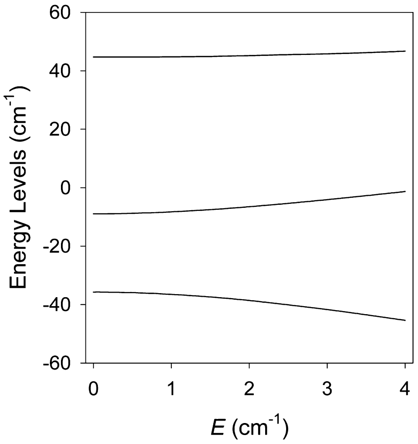

Figure 4. Effect of the E parameter on the energy levels of an S = 5/2 system with ZFS parameters of D = 13.4 and E = 0.3 cm^{-1} (in [Fe(TPP)I]).

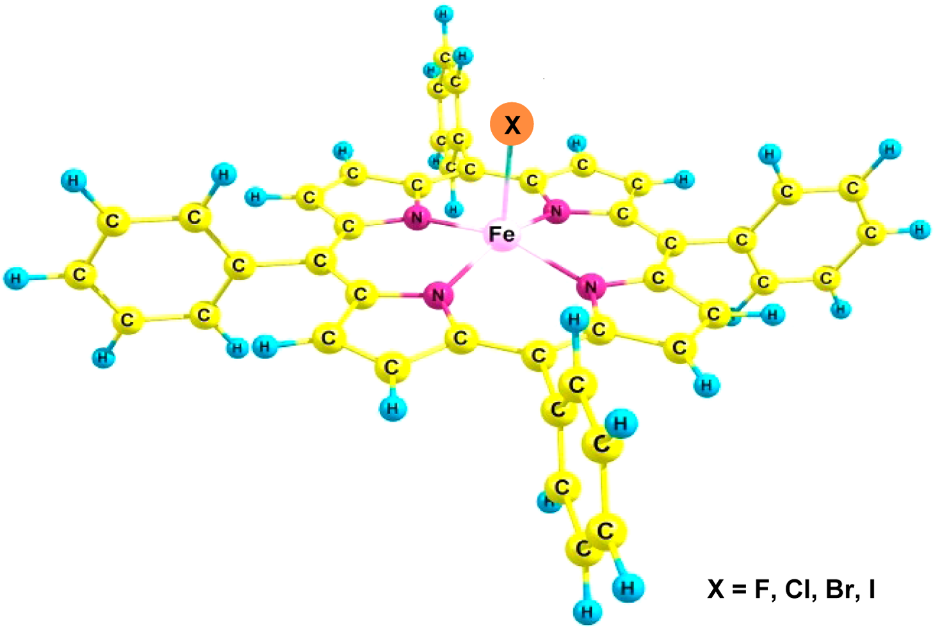

Figure 5. Structural view of the series of complexes as revealed by X-ray and neutron diffraction studies and DFT geometry optimizations.

deuteroporphyrin IX dimethyl ester halides are also summarized there. Several methods gave D = 3.2−11.9 cm^{-1} for [Fe(TPP)Cl] and 4.9−12.5(5) cm^{-1} for [Fe(TPP)Br]. Our INS studies[11] gave accurate values for the complexes. It is also interesting to note that the D values for [Fe(TPP)X] are similar to those of the corresponding Fe(III) protoporphyrin IX dimethyl ester halides (Table 1).

Calculated Coordination Geometries. The geometries of the first-coordination spheres of the four [Fe(TPP)X] complexes are square pyramidal (Figure 5) with four equatorial Fe−N and one axial Fe−X bond. Structural parameters from X-ray data are well reproduced by the DFT geometry optimization (Table 2). The set of Cartesian coordinates for each DFT optimized structure is listed in the Supporting Information.

Multiplet Energies and the Zero-Field Splitting (*D*). From CASSCF and NEVPT2 calculations for [Fe(TPP)X] at DFT-optimized geometries, we can conclude that all four complexes are in a $^6A_1$ ground state. Quartet ($S = 3/2$) excited states originate from the ^4G, ^4D, ^4F, and ^4P states of the free Fe(III) ion split by the C_{4v} ligand field in the complex. Energies of CASSCF and NEVPT2 of these terms in the energy range below 50 000 cm^{-1} are included in Tables S5 and S6. From all of these, the states with the $^4T_1$ cubic parentage split into ^4E and $^4A_2$ terms. Their mixing with the $^6A_1$ ground state via spin−orbit coupling leads to splitting of its $M_s = \pm 5/2, \pm 3/2$, and $\pm 1/2$ sublevels, thus governing the sign and magnitude of the zero-field splitting terms. From the three $^4T_1$ cubic terms, only two yield essential contributions to D. Their energies and calculated D values are depicted in Figure 6. Second-order perturbation theory yields the following $^6A_1$ ground-state expression for D:

$$D(^4T_1) = \frac{\varsigma_{\text{eff}}^2}{5}\left[\frac{1}{\Delta(^4A_2)} - \frac{1}{\Delta(^4E)}\right] \tag{3}$$

where ς_{eff} is the effective SOC constant and $\Delta(^4A_2)$ and $\Delta(^4E)$ are the energies of the ^4E and $^4A_2$ C_{4v} sublevels of each $^4T_1$ term.

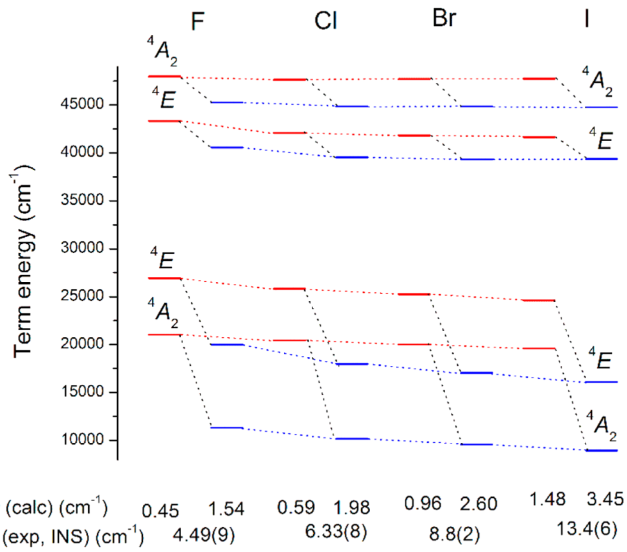

Figure 6. Term energies from CASSCF and NEVPT2 calculations governing the sign and magnitude of the $^6A_1$ ground state D value of the series of [Fe(TPP)X] (X = F, Cl, Br, I) complexes; color code: red, CASSCF; blue, NEVPT2.

From eq 3, it is evident that when the energy of the ^4E excited state is greater than that of the $^4A_2$ excited state (Figure 6) from the lowest cubic $^4T_1$ term, a positive D value results, while if the energy of the excited states is reversed ($^4E < {}^4A_2$), a negative D value results. Because of the larger $^4T_1$−$^6A_1$ energy separation for the second excited $^4T_1$ state, the positive term dominates and determines the positive sign of D for the entire complex. Qualitative predictions of the positive sign of D for such coordination geometries of Fe(III) using angular overlap model consideration have been published.[50]

In Figure 6 and Table 3, we compare calculated and experimental values of D. While the experimental trend D(F) < D(Cl) < D(Br) < D(I) is well reproduced, computed CASSCF values of D are about 1 order of magnitude (8−10) smaller than the experimental values. This can be attributed to the ionic

Table 3. Metal–Ligand Bonding and Electron Repulsion Parameters for the [Fe(TPP)X] (X = F, Cl, Br, I, DFT Optimized Structures) Series (in $\mathrm{cm^{-1}}$) from Ab Initio Ligand Field Analysis and a Best Fit of the Angular Overlap Model to the CASSCF/NEVPT2 (CAS(5,5) Active Space) Quartet Excited-State Energies

X	F		Cl		Br		I	
ligand field parameters	CASSCF	NEVPT2 (C%)[b]	CASSCF	NEVPT2	CASSCF	NEVPT2	CASSCF	NEVPT2
e_σ^{X}[a]	6260	7355 (15)	4200	5348 (21)	3358	4501 (25)	2798	4055 (31)
e_π^{X}[a]	2340	2625 (11)	1177	1287 (8)	843	873 (3)	523	474 (−10)
e_σ^{N}[a]	5650	6058 (7)	5784	6266 (8)	5862	6372 (8)	5930	6467 (8)
B	1145	1032	1127	1023	1122	1022	1114	1018
(B/B_0)[c]	0.88	0.83	0.87	0.82	0.86	0.82	0.85	0.82
C	4297	4698	4231	4735	4219	4761	4197	4800
(C/C_0)[c]	0.89	1.05	0.87	1.05	0.87	1.06	0.87	1.07
ζ	436	436	429	429	415	415	392	392
(ζ/ζ_o)[c]	0.92	0.92	0.91	0.91	0.88	0.88	0.83	0.83
D (calc)	0.45	1.54	0.59	1.98	0.96	2.60	1.48	3.45
D (exp, INS)	4.49(9)		6.33(8)		8.8(2)		13.4(6)	

[a] Parameterization was done under the following simplifying assumptions: $e_{\pi s}^{N} = e_{\pi c}^{N} = 0$. [b] Percentage covalence C%, defined as $\{[e_\lambda(\mathrm{NEVPT2}) - e_\lambda(\mathrm{CASSCF})]/e_\lambda(\mathrm{NEVPT2})\} \times 100$ ($\lambda = \sigma, \pi$), is listed in brackets. (See ref 47, p 187 for details.) [c] Nephelauxetic ratios of the Racah parameters B, C and the spin–orbit coupling parameter ζ in the complex with respect to the computed values B_0, C_0, and ζ_o for the free Fe(III) ion: 1301, 4844, 472 (CASSCF) and 1240, 4490, 472 $\mathrm{cm^{-1}}$ (NEVPT2), respectively.

nature of the CASSCF wave functions where metal–ligand covalence is largely underestimated. In agreement with this result, dynamical correlation accounted for by NEVPT2 improves the quantitative agreement with the experimental data; now D(NEVPT2) values differ by a factor of 3–4 as compared to the experimental ones. This will be thoroughly discussed in a separate section below. The changes from the CASSCF to NEVPT2 results are reflected by the drop down in energy of the $^4A_2$ and ^4E lowest excited states by as much as 10 000 $\mathrm{cm^{-1}}$ and by about one-half this amount for the second excited state of the same C_{4v} symmetry. The trends in D across the series are nicely reflected by the concerted lowering of the transitions energies from F to I in the series. The contributions to D from the two $^4T_1$ states (Tables S5 and S6 in comparison with eq 3) show that the improvement of the D parameters upon NEVPT2 corrections is largely dominated by the lowest $^4T_1$ term and the lowering of the excitation energy to $^4A_2$ (by about 10 250 $\mathrm{cm^{-1}}$), which exceeds the energy lowering of the higher, excited ^4E state (by about 7800 $\mathrm{cm^{-1}}$). This is a differential correlation effect, which increases with Fe–X covalence increasing in the series F, Cl, Br, and I.

A calibration of the CASSCF and NEVPT2 values of D allows one to predict the experimental D starting from the computed ones. The latter are compared to the experimental D values in Figure 7. A least-squares fit between the experimental and the theoretical D values leads to the following expressions:

$$D(\mathrm{exp\ ,\ INS}) = 8.326D(\mathrm{CASSCF}) + 0.997\ (\mathrm{cm^{-1}}) \tag{4}$$

$$D(\mathrm{exp\ ,\ INS}) = 4.625D(\mathrm{NEVPT2}) - 2.8255\ (\mathrm{cm^{-1}}) \tag{5}$$

with a standard deviation of 0.18 $\mathrm{cm^{-1}}$ between the two data sets.

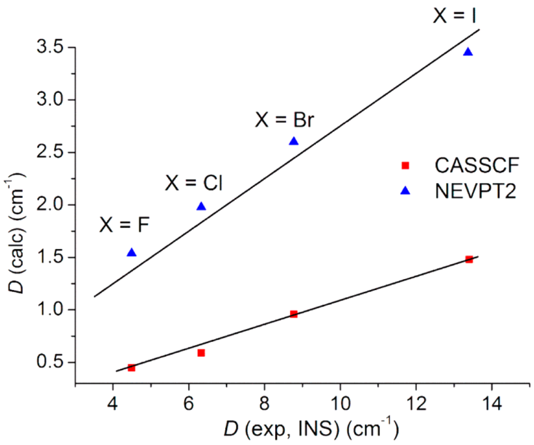

Figure 7. Calibration between experimental and CASSCF/NEVPT2 calculated values of the zero-field splitting parameter D for the [Fe(TPP)X] series; D (exp, INS) = 8.326D(CASSCF) + 0.997, standard deviation = 0.18 $\mathrm{cm^{-1}}$; D (exp, INS) = 4.625D(NEVPT2) − 2.8255, standard deviation = 0.18 $\mathrm{cm^{-1}}$.

Metal–Ligand Bonding from Angular Overlap Ligand Field Analysis of the CASSCF and NEVPT2 Many-Electron States and the Correlation with *D*. Bonding in [Fe(TPP)X] is governed by two types of donors: the equatorial nitrogen of the TPP and axial X ligands. Angular overlap expressions for the energies of 3d-type MOs in the simple case of square-pyramidal FeN_4X with ligands at the x,y and z axes are given by

$$\begin{aligned} e(b_1, d_{x2-y2}) &= 3e_\sigma^{N} \\ e(a_1, d_{z2}) &= e_\sigma^{X} + e_\sigma^{N} - 4e_{sd}^{N} - e_{sd}^{X} + 4(e_{sd}^{X}e_{sd}^{N})^{1/2} \\ e(e, d_{xz,yz}) &= e_\pi^{X} + 2e_{\pi\perp}^{N} \\ e(b_2, d_{xy}) &= 4e_{\pi\|}^{N} \end{aligned} \tag{6}$$

Two sets of parameters e_σ^{N}, e_σ^{X} and e_π^{N}, e_π^{X} are introduced to account for σ and π-antibonding, with $e_{\pi\|}^{N}$ and $e_{\pi\perp}^{N}$ describing iron–nitrogen in- and out-of-plane π-interactions, respectively. The parameters e_{sd}^{N} and e_{sd}^{X} account for the stabilization of the $d_z{}^2$ orbital due to partial hybridization with the 4s one. The mixing of these two orbitals is induced by the 4-fold symmetry where both orbitals are of the a_1 type. Because the N atoms of

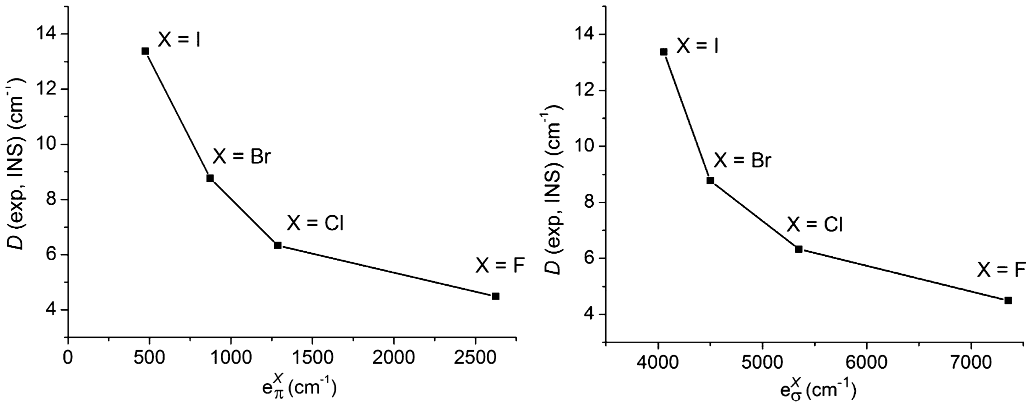

Figure 8. Magneto-structural correlation between the experimental D values and the Fe−X π (left) and σ (right) antibonding energies as given by a best fit of the angular overlap plus repulsion ligand field model to NEVPT2 eigenvalues.

the porphyrin ligand do not possess electrons for in-plane π-bonding, $e_{\pi\|}^{N}$ can be safely set to zero. Even so, one is left with six parameters from which only three are independent in the given point group. To achieve further realistic approximation to reduce the number of parameters, we considered a Fe(TPP)$^+$ complex without the X atom. For such a complex (D_{4h} symmetry), eq 6 is simplified to

$$
\begin{aligned}
e(\mathrm{b}_1, \mathrm{d}_{x2-y2}) &= 3e_\sigma^{N} \\
e(\mathrm{a}_1, \mathrm{d}_{z2}) &= e_\sigma^{N} - 4e_{\mathrm{sd}}^{N} \\
e(\mathrm{e}, \mathrm{d}_{xz,yz}) &= 2e_{\pi\perp}^{N} \\
e(\mathrm{b}_2, \mathrm{d}_{xy}) &= 0
\end{aligned}
\tag{7}
$$

A best fit of e_σ^N, $e_{\pi\perp}^N$, and e_{sd}^N and B to energy eigenvalues from CASSCF calculations of a Fe(TPP)$^+$ model complex resulted, respectively, in values of 5725, 99, 1289, and 990 cm^{-1}. These results show that while keeping to an approximate CASSCF wave function, $e_{\pi\perp}^N$ can be safely neglected. We thus arrive at a model with three parameters e_σ^N, e_σ^X, and e_π^X, where e_{sd}^N and e_{sd}^X have been neglected. Parameters e_σ^N, e_σ^X, e_π^X, B and C have been obtained from a best fit to energies from CASSCF and NEVPT2 calculations for transitions from the $^6A_1$ ground into the $S = 3/2$ excited states (Table 3). In this procedure, the detailed angular geometry as given by the DFT structure optimizations was taken into account. While the energy of the Fe−N antibonding e_σ^N is almost constant between the various members, e_σ^X and e_π^X decrease across the series from F to I and thus correlate with the increase of D in the same direction (Figure 8). The bonding parameters from Table 3 have been used to deduce the ligand field splitting pattern of the 3d-MOs (Figure 9), which we in turn employ to rationalize D versus e_π^X and e_σ^X correlation. According to eq 3, the value of D is dominated by contributions from ^4E and $^4A_2$ terms for the lower and the upper $^4T_1$ states. All four transitions are governed by an increase of interelectronic repulsion when going from the $^6A_1$ ground state (five unpaired electrons on each 3d MO) into excited states with electronic configurations, where one orbital becomes doubly occupied (an energy that equals roughly $10B + 6C$ for both $^4T_1$ states). Excitations from the $^6A_1$ ground state into the lower ^4E and $^4A_2$ pair correspond to $e \rightarrow t_2$ transitions with a gain of ligand field energy (ligand field de-excitation). As illustrated in Figure 9 (middle left), this gain is larger for the $^4A_2$ state than for the ^4E state, leading to an energy ordering $\Delta(^4E) > \Delta(^4A_2)$ and, according to eq 3, a positive contribution to D. Transitions to the upper $^4T_1$ state are of the $t_2 \rightarrow e$ type. Therefore, when exciting from $^6A_1$, they are adding energy to the $10B + 6C$ term. According to Figure 9 (middle, right), a $\Delta(^4E) < \Delta(^4A_2)$ term sequence for the upper $^4T_1$ state leads to a negative contribution to D. Coming from a lower lying transition, positive contributions to D clearly dominate and determine the overall sign of D. With e_σ^X and e_π^X decreasing across the series X = F to I, both $^4A_2$, the lowest excited state, and ^4E, the second excited state, become lower in energy. However (Table S5), the changes of the energy of $^4A_2$ dominate over those of ^4E and are mainly responsible for the observed increase in D. As shown in a comparison between the CASSCF and NEVPT2 results in Tables S5 and S6, the effect is enhanced when taking dynamical correlation into account.

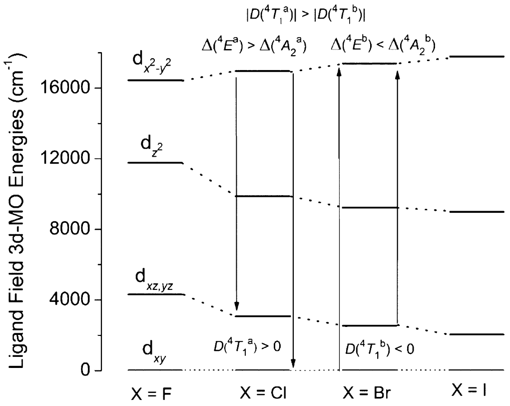

Figure 9. Ligand field 3d-MO energies from ab initio (NEVPT2) calculations of the [Fe(TPP)X] series.

Magnetic Anisotropy (*D*) and Metal−Ligand Covalence in the [Fe(TPP)X] Series. Changes in covalence in 3d complexes affect D: (1) decrease in the spin−orbit coupling (SOC, quantified by ζ) reduces D, eq 3; and (2) reduction the interelectronic repulsion (quantified by the Racah parameters B and C) with respect to the free ions (nonrelativistic and relativistic nephelauxetic effects, respectively) increases D. Ab initio ligand field analyses clearly manifest a decrease of B and ζ across the series (Table 3, CASSCF/NEVPT2 results), reflecting the expected increase of metal−ligand covalence from F to I, as shown in Figure S20. It is worth considering these two effects on D separately.

Effect of Spin−Orbit Coupling (SOC) on *D*. Desrochers and co-workers studied ZFS in 4-coordinate C_{3v} Ni(II) complexes Tp*NiX [Tp*$^-$ = hydrotris(3,5-dimethylpyrazole)-borate; X = Cl, Br, I] by HFEPR, reporting $D = +3.93(2)$, −11.43(3), −22.81(1) cm^{-1}, for X = Cl, Br, I, respectively, for the d^8 $S = 1$ complexes.[51] Studies by the Angular Overlap Model (AOM)[51] and wave function-based ab initio methods[52] show that the final signs and magnitudes of D parameters here are mostly determined by the metal−ligand covalency and low symmetry in the scorpionate complexes. These 4-coordinate, d^8 Ni(II) complexes are more covalent than the 5-coordinate, high-spin d^5 [Fe(TPP)X] in the current work. Theoretical studies of $[NiX_4]^{2-}$ (X = F, Cl, Br, I) also showed the increasing contribution of intraligand spin−orbit coupling to ZFS from F, Cl, Br to I in $[NiX_4]^{2-}$, leading to a sign reversal, between Br and I, of the spin−orbit splitting within the t$_2$-orbitals of Ni^{2+} ions.[53] Being relatively more ionic, the effect of the intrinsic spin−orbit couplings of the heavier ligands on D in the [Fe(TPP)X] series is not as strong as that in the Tp*NiX or $[NiX_4]^{2-}$ complexes. In other words, the $\{Fe^{III}{-}X^-\}^7 \rightarrow \{Fe^{II}{-}X^\bullet\}^7$ charge transfer is much higher in energy than $\{Ni^{II}{-}X^-\}^{10} \rightarrow \{Ni^{I}{-}X^\bullet\}^{10}$ so that the large SOC of I$^-$ cannot affect D considerably. Although the N atoms (on the porphyrin ligand) and halides X in [Fe(TPP)X] are involved in strong σ bonding with Fe(III) (as quantified by the parameters e_σ^N and e_σ^X in eq 6), there is no first-order spin−orbit coupling in the $^6A_1$ ground state. Thus, the impact of all of these factors on the ZFS of the [Fe(TPP)X] series is not as large as in the Ni(II) complexes.

Effect of the Nephelauxetic Reduction of *B* and *C* on *D*. D values of axial Fe^{III} complexes are generally underestimated by both CASSCF and NEVPT2 methods. Correlation effects in the $S = 5/2$ ground state and $S = 3/2$ excited state are quite different. Dynamical correlation in the latter states is much more pronounced and is largely underestimated at both the CASSCF and the NEVPT2 level of theories. This differential correlation effect results in interelectronic repulsion parameters B and C distinctly larger than those deduced from experiment. This leads to (a) a larger gap between the $^6A_1$ ground state and the $^4A_2/^4E$ excited states; and (b) small values of D according to eq 3. To quantify the effect, we have adapted the angular overlap model with parameters from Table 3 and studied the dependence of D on B, while keeping the ratio C/B unchanged. A model calculation for [Fe(TPP)Cl] as an example shows a dramatic increase of D when lowering B (Figure 10). Such (nephelauxetic) reduction of B is a measure of metal−ligand covalence. The rather large values of B deduced from the multireference ab initio calculations (1000−1100 cm^{-1}) reflect the rather ionic CASSCF wave functions. Because of this ionicity, the nephelauxetic reduction of B is largely underestimated at the ab initio level. The effect can be quantified by getting B that reproduces D from the INS work. Adapting again the angular overlap model with the same values of the parameters for the complexes (Table 3, NEVPT2 set), we obtain $B = 579$ (F), 557 (Cl), 540 (Br), and 518 (I) cm^{-1}. In other words, they are twice as small as their ab initio counterparts (both CASSCF and NEVPT2, Table 3). Taking this result with precaution (due to the model character of the given considerations), we can conclude that the reduction of B is largely governed by the TPP ligand and further modified by the covalence of the Fe−X bond increasing from F to I. Finally, the large reduction of the parameters B deduced from the INS data implies a shift of the electronic transitions $^6A_1 \rightarrow {}^4A_2$ ($^4T_1$) and $^6A_1 \rightarrow {}^4E$ ($^4T_1$) from their ab initio values [NEVPT2: 11 135 and 20 006 (F) to 8960 and 16 089 cm^{-1} (I), Table S6] to the near-IR and IR regions [explicitly: 4738/8878 (F), 3685/9035 (Cl), 2738/7652 (Br), and 1719/6135 (I)]. Thus, these transitions are falling in energy below the Soret (∼24 000 cm^{-1}) and Q-bands (16 000−20 000 cm^{-1})[54] π−π* absorption region. This opens an interesting perspective for their spectroscopic characterization.

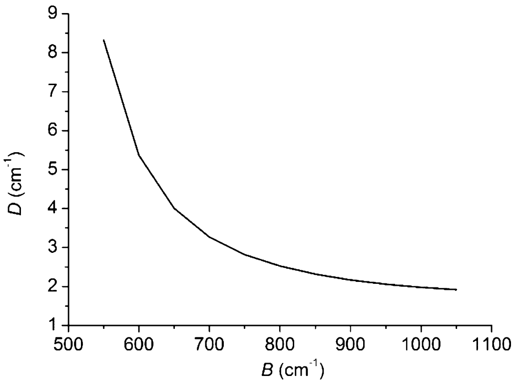

Figure 10. Variation of D with B for [Fe(TPP)Cl] taken as a model example. The figure has been constructed using the AOMX program package with model parameters set (NEVPT2) from Table 3. A C/B ratio of 4.63 has been adapted using the same data.

■ CONCLUDING REMARKS

Zero-field splittings in [Fe(TPP)X] (X = F, Br, I) have been studied by inelastic neutron scattering, providing a rare, complete determination of ZFS parameters in a metalloporphyrin halide series. Ligand field analysis of the ab initio data shows that the relatively large D values for these complexes are due to delocalization of the σ d-electrons on the TPP ligand, which lowers the parameter B and reduces the energy gap between the ground $^6A_1$ ground and the $^4A_2$ excited state. The trend of the increase in D, from X = F, Cl, Br, to I, is further correlated with the increase in the covalency of the Fe−X bond in the same order. Ab initio multireference electronic structure calculations and their ligand field analysis allow one to relate the increase in the D values with the lowering of the energy gap between the $^6A_1$ ground state and the $^4T_1$ lowest excited state. This lowering is attributed to the weakening of both the σ and the π antibonding interactions between the Fe(III) ion and the axial halide ligand. Quantitative magneto-structural correlations were derived between D and the angular overlap model parameters e_σ and e_π, characterizing the bonds of iron(III) ion to the axial ligands.

Single ion magnets (SIMs) are of intense current interest. There is a significant debate regarding the strategy for the design and synthesis of SIMs. To rationally design SIMs, key factors dictating the sign and magnitude of D values in metal complexes need to be identified. The current work not only reports ZFS parameters by inelastic neutron scattering for the 5-coordinate halide complexes, but also identifies key factors that determine the sign and magnitude of D values in these Fe^{III} single ion complexes.

An important point we learn from the current study is that, for square pyramidal 5-coordinate high-spin d^5 complexes, D may become negative if the equatorial ligand donors are weaker than the axial one.

■ ASSOCIATED CONTENT

Ⓢ Supporting Information

The Supporting Information is available free of charge on the ACS Publications website at DOI: 10.1021/acs.inorgchem.5b01505.

> UV–visible spectra of [Fe(TPP)X] (X = F, Br, I), XRD analyses of the samples, elemental analyses of [Fe(TPP)X] (X = Br, I), error analyses of the INS spectra, experimental and calculated intensities of INS peaks, Q dependence plots, tables of quartet excited-state energies (in cm^{-1}) from CASSCF and NEVPT2/CASSCF calculations with an active space of five d-electrons distributed of the five 3d MOs [CAS(5,5)] for [Fe(TPP)X], and Cartesian coordinates resulting from DFT geometry optimizations of the [Fe(TPP)X] series (PDF)

■ AUTHOR INFORMATION

Corresponding Authors

*E-mail: mihail.atanasov@cec.mpg.de.
*E-mail: podlesnyakaa@ornl.gov.
*E-mail: frank.neese@cec.mpg.de.
*E-mail: xue@utk.edu.

Notes

The authors declare no competing financial interest.

■ ACKNOWLEDGMENTS

The work is supported by the U.S. National Science Foundation (CHE-1362548 to Z.-L.X.). Acknowledgment is also made to the Donors of the American Chemical Society Petroleum Research Fund for partial support of this research. Research at Oak Ridge National Laboratory's Spallation Neutron Source was supported by the Scientific User Facilities Division, Office of Basic Energy Sciences, U.S. Department of Energy. We acknowledge the technical and scientific support from the staff at the SNS. We thank Dr. Jurek Krzystek (National High Magnetic Field Laboratory, Florida State University) and Prof. Joshua Telser (Roosevelt University) for helpful discussions and for communicating HFEPR results on the Fe(TPP)X complexes.

■ REFERENCES

(1) *The Porphyrin Handbook*; Kadish, K. M., Smith, K. M., Guilard, R., Eds.; Academic Press: San Diego, CA, 2000–2003.

(2) For geochemistry of porphyrins, see, for example: Callot, H. J.; Ocampo, R. *The Porphyrin Handbook*; Academic Press: San Diego, CA, 2000; Vol. *1*, Chapter 7, pp 349–398.

(3) (a) Hoffman, B. M. *Proc. Natl. Acad. Sci. U. S. A.* **2003**, *100*, 3575. (b) Yang, F.; Shokhireva, T. K.; Walker, F. A. *Inorg. Chem.* **2011**, *50*, 1176. (c) Scheidt, W. R.; Barabanschikov, A.; Pavlik, J. W.; Silvernail, N. J.; Sage, J. T. *Inorg. Chem.* **2010**, *49*, 6240. (d) de Visser, S. P.; Valentine, J. S. V.; Humphreys, K. J. *Pure Appl. Chem.* **1998**, *70*, 855. (e) Zhang, P.; Wang, M.; Li, X.; Qiang, C.; Hong, G.; Dong, J. F.; Sun, L. C. *Sci. China: Chem.* **2012**, *55*, 1274.

(4) (a) Boca, R. *Coord. Chem. Rev.* **2004**, *248*, 757. (b) Neese, F.; Solomon, E. I. In *Magnetism*; Miller, J. S., Drillon, M., Eds.; Wiley-VCH: New York, 2003; Vol. *IV*, pp 345–466. (c) Long, J. R. In *Chemistry of Nano-structured Materials*; Yang, P., Ed.; World Scientific: Hong Kong, 2003; pp 291–315.

(5) Deaton, J. C.; Gebhard, M. S.; Solomon, E. I. *Inorg. Chem.* **1989**, *28*, 877.

(6) Browett, W. R.; Fucaloro, A. F.; Morgan, T. V.; Stephens, P. J. *J. Am. Chem. Soc.* **1983**, *105*, 1868.

(7) Because the electronic excited states are much higher in energy than the ground state, fourth-rank terms given by fourth-order perturbation theory are neglected here.

(8) Gatteschi, D.; Sessoli, R. *Angew. Chem., Int. Ed.* **2003**, *42*, 268.

(9) Nehrkorn, J.; Telser, J.; Holldack, K.; Stoll, S.; Schnegg, A. *J. Phys. Chem. B* **2015**, article ASAP; http://pubs.acs.org/doi/pdfplus/10.1021/acs.jpcb.5b04156.

(10) (a) *Applications of Physical Methods to Inorganic and Bioinorganic Chemistry*; Scott, R. A., Lukehart, C. M., Eds.; Wiley: New York, 2007; including Larese, J. Z., pp 291–313. (b) Gatteschi, D. *J. Phys. Chem. B* **2000**, *104*, 9780. (c) Krzystek, J.; Ozarowski, A.; Telser, J. *Coord. Chem. Rev.* **2006**, *250*, 2308.

(11) Hunter, S. C.; Podlesnyak, A. A.; Xue, Z.-L. *Inorg. Chem.* **2014**, *53*, 1955.

(12) Brackett, G. C.; Richards, P. L.; Caughey, W. S. *J. Chem. Phys.* **1971**, *54*, 4383.

(13) Goff, H. M.; Shimomura, E. T.; Phillippi, M. A. *Inorg. Chem.* **1983**, *22*, 66.

(14) Ohya, T.; Sato, M. *J. Chem. Soc., Dalton Trans.* **1996**, 1519.

(15) (a) Behere, D. V.; Date, S. K.; Mitra, S. *Chem. Phys. Lett.* **1979**, *68*, 544. (b) Maricondi, C.; Swift, W.; Straub, D. K. *J. Am. Chem. Soc.* **1969**, *91*, 5205.

(16) Behere, D. V.; Birdy, R.; Mitra, S. *Inorg. Chem.* **1981**, *20*, 2786.

(17) Uenoyama, H. *Biochim. Biophys. Acta, Gen. Subj.* **1971**, *230*, 479.

(18) (a) Furrer, A. *Int. J. Mod. Phys. B* **2010**, *24*, 3653. (b) Andres, H.; Basler, R.; Güdel, H.-U.; Aromi, G.; Christou, G.; Büttner, H.; Ruffle, B. *J. Am. Chem. Soc.* **2000**, *122*, 12469. (c) Basler, R.; Sieber, A.; Chaboussant, G.; Güdel, H. U.; Chakov, N. E.; Soler, M.; Christou, G.; Desmedt, A.; Lechner, R. *Inorg. Chem.* **2005**, *44*, 649. (d) Kittilstved, K. R.; Sorgho, L. A.; Amstutz, N.; Tregenna-Piggott, P. L. W.; Hauser, A. *Inorg. Chem.* **2009**, *48*, 7750. (e) Wang, C. H.; Lumsden, M. D.; Fishman, R. S.; Ehlers, G.; Hong, T.; Tian, W.; Cao, H.; Podlesnyak, A.; Dunmars, C.; Schlueter, J. A.; Manson, J. L.; Christianson, A. D. *Phys. Rev. B: Condens. Matter Mater. Phys.* **2012**, *86*, 064439/1. (f) Carver, G.; Tregenna-Piggott, P. L. W.; Barra, A.-L.; Neels, A.; Stride, J. A. *Inorg. Chem.* **2003**, *42*, 5771. (g) Dreiser, J.; Waldmann, O.; Dobe, C.; Carver, G.; Ochsenbein, S. T.; Sieber, A.; Güdel, H. U.; van Duijn, J.; Taylor, J.; Podlesnyak, A. *Phys. Rev. B: Condens. Matter Mater. Phys.* **2010**, *81*, 024408.

(19) Ehlers, G.; Podlesnyak, A.; Niedziela, J. L.; Iverson, E. B.; Sokol, P. E. *Rev. Sci. Instrum.* **2011**, *82*, 085108.

(20) Alder, A. D.; Longo, F. R.; Kampas, F.; Kim, J. *J. Inorg. Nucl. Chem.* **1970**, *32*, 2443.

(21) Hunter, S. C.; Smith, B. A.; Hoffmann, C. M.; Wang, X.; Chen, Y.-S.; McIntyre, G. J.; Xue, Z.-L. *Inorg. Chem.* **2014**, *53*, 11552.

(22) Anzai, K.; Hatano, K.; Lee, Y. J.; Scheidt, W. R. *Inorg. Chem.* **1981**, *20*, 2337. The cif file from http://www.ccdc.cam.ac.uk on Jan. 24, 2015 does not contain atom coordinates.10.1021/ic50221a079

(23) Le Bail, A. *Powder Diffr.* **2004**, *19*, 249.

(24) (a) Skelton, B. W.; White, A. H. *Aust. J. Chem.* **1977**, *30*, 2655. (b) For the conversion of the space group from the reported $P2_1/c$ to $P2_1/n$, see: Feast, G. C.; Haestier, J.; Page, L. W.; Robertson, J.; Thompson, A. L.; Watkin, D. J. *Acta Crystallogr., Sect. C: Cryst. Struct. Commun.* **2009**, *65*, o635 and the matrix and software at http://www.cryst.ehu.es/cryst/celltran.html.10.1107/S0108270109046952

(25) Hatano, K.; Scheidt, W. R. *Inorg. Chem.* **1979**, *18*, 877.

(26) Basler, R.; Boskovic, C.; Chaboussant, G.; Güdel, H. U.; Murrie, M.; Ochsenbein, S. T.; Sieber, A. *ChemPhysChem* **2003**, *4*, 910.

(27) Furrer, A.; Mesot, J.; Strässle, T. *Neutron Scattering in Condensed Matter Physics*; World Scientific: NJ, 2009; p 17.

(28) Azuah, R. T.; Kneller, L. R.; Qiu, Y.; Tregenna-Piggott, P. L. W.; Brown, C. M.; Copley, J. R. D.; Dimeo, R. M. *J. Res. Natl. Inst. Stand. Technol.* **2009**, *114*, 341.

(29) Grimme, S.; Antony, J.; Ehrlich, S.; Krieg, H. *J. Chem. Phys.* **2010**, *132*, 154104.

(30) Grimme, S.; Ehrlich, S.; Goerigk, L. *J. Comput. Chem.* **2011**, *32*, 1456.

(31) Pantazis, D. A.; Chen, X. Y.; Landis, C. R.; Neese, F. *J. Chem. Theory Comput.* **2008**, *4*, 908.

(32) Malmqvist, P.-Å; Roos, B. O. *Chem. Phys. Lett.* **1989**, *155*, 189.
(33) Angeli, C.; Cimiraglia, R.; Malrieu, J.-P. *Chem. Phys. Lett.* **2001**, *350*, 297.
(34) Angeli, C.; Cimiraglia, R.; Evangelisti, S.; Leininger, T.; Malrieu, J.-P. *J. Chem. Phys.* **2001**, *114*, 10252.
(35) Angeli, C.; Cimiraglia, R.; Malrieu, J.-P. *J. Chem. Phys.* **2002**, *117*, 9138.
(36) Borini, S.; Cestari, M.; Cimiraglia, R. J. *J. Chem. Phys.* **2004**, *121*, 4043.
(37) Angeli, C.; Bories, B.; Cavallini, A.; Cimiraglia, R. *J. Chem. Phys.* **2006**, *124*, 54108.
(38) Neese, F. *WIREs Comput. Mol. Sci.* **2012**, *2*, 73.
(39) Neese, F. with contributions from Becker, U.; Ganyushin, G.; Hansen, A.; Izsak, R.; Liakos, D. G.; Kollmar, C.; Kossmann, S.; Pantazis, D. A.; Petrenko, T.; Reimann, C.; Riplinger, C.; Roemelt, M.; Sandhöfer, B.; Schapiro, I.; Sivalingam, K.; Wennmohs, F.; Wezisla, B.; and contributions from our collaborators Kállay, M.; Grimme, S.; Valeev, E. *ORCA - An ab initio, DFT and Semiempirical SCF-MO Package*, Version 3.0; Mülheim a.d.R. The binaries of ORCA are available free of charge for academic users for a variety of platforms.
(40) Atanasov, M.; Ganyushin, D.; Pantazis, D. A.; Sivalingam, K.; Neese, F. *Inorg. Chem.* **2011**, *50*, 7460.
(41) Neese, F. *J. Chem. Phys.* **2005**, *122*, 34107.
(42) Ganyushin, D.; Neese, F. *J. Chem. Phys.* **2006**, *125*, 024103.
(43) Schaefer, A.; Horn, H.; Ahlrichs, R. *J. Chem. Phys.* **1992**, *97*, 2571.
(44) Weigend, F.; Ahlrichs, R. *Phys. Chem. Chem. Phys.* **2005**, *7*, 3297.
(45) Jørgensen, C. K.; Pappalardo, R.; Schmidtke, H.-H. *J. Chem. Phys.* **1963**, *39*, 1422.
(46) Schäffer, C. E.; Jørgensen, C. K. *Mol. Phys.* **1965**, *9*, 401.
(47) Atanasov, M.; Ganyushin, D.; Sivalingam, K.; Neese, F. *Struct. Bonding (Berlin, Ger.)* **2012**, *143*, 149.
(48) Atanasov, M.; Zadrozny, J. M.; Long, J. R.; Neese, F. *Chem. Sci.* **2013**, *4*, 139.
(49) Adamsky, H. *AOMX, a FORTRAN Program for the Calculation of* d^n *Terms within the Angular Overlap Model with Interelectronic Repulsion and Spin-Orbit Coupling*; Institute of Theoretical Chemistry, Heinrich-Heine-University: Düsseldorf, 1995. This program, both executable and source code, is freely distributable by M.A. upon request.
(50) Gatteschi, D.; Sorace, L. *J. Solid State Chem.* **2001**, *159*, 253.
(51) Desrochers, P. J.; Telser, J.; Zvyagin, S. A.; Ozarowski, A.; Krzystek, J.; Vicic, D. A. *Inorg. Chem.* **2006**, *45*, 8930.
(52) Ye, S.; Neese, F. *J. Chem. Theory Comput.* **2012**, *8*, 2344.
(53) Atanasov, M.; Rauzy, C.; Baettig, P.; Daul, C. *Int. J. Quantum Chem.* **2005**, *102*, 119.
(54) Sun, Z.-C.; She, Y.-B.; Zhou, Y.; Song, X.-F.; Li, K. *Molecules* **2011**, *16*, 2960.

DOI: 10.1021/acs.inorgchem.5b01505
Inorg. Chem. XXXX, XXX, XXX−XXX